Journal of Sound and Vibration (2001) **239**(3), 423–443
doi:10.1006/jsvi.2000.3141, available online at http://www.idealibrary.com on IDEAL®

THE EFFECTS OF DISCONTINUOUS BOUNDARY CONDITIONS ON THE DIRECTIVITY OF SOUND FROM A PISTON

C. CHEONG AND S. LEE

Seoul National University, Shinrim-Dong, Kwanak-Ku, Seoul 151-742, *South Korea*

(*Received* 30 *August* 1999, *and in final form* 1 *June* 2000)

The radiation patterns of sound from a baffled, oscillating piston are studied via a numerical method. To investigate the effects of discontinuous boundary condition on the sound radiation from a piston, we introduce three piston models that have, respectively, definite characteristics at their own edges. Linearized Euler's equations in Cartesian co-ordinates are solved by the dispersion relation preserving finite difference scheme. The numerical results are compared with the analytic results derived from the Kirchhoff–Helmholtz integral theorem. Through the comparison of numerical results of each boundary condition, we find that discontinuity at the edge of the piston as well as the Helmholtz number of the vibrating piston is an important factor in determining the sound radiation pattern of the piston. The validity of numerical simulation for discontinuity effects is confirmed by comparison of the numerical and analytic results.

1. INTRODUCTION

A good understanding of the geometry effect on noise propagation is of great importance to noise control, especially in duct acoustics. It is well known that the directivity pattern of the radiated noise consists of lobes (high intensity) and nodes (region of relative silence) due to the refraction of the outgoing acoustic waves at the rim of an open end of the duct. Theoretical methods [1–5] via Wiener–Hopf and other techniques have been very successful in studying ducted acoustics radiation for flat ducts with zero thickness. Recently, Dong *et al.* performed direct numerical simulations of noise radiation from ducts with various geometries [6]. Tam also investigated the influence of nozzle geometry on the noise of high-speed jets with experimental data [7]. Their studies, however, were on the geometry-affected response characteristics of noise and not on its intrinsic mechanism.

Sound radiation from a vibrating circular piston is a classical acoustics problem. An expression for the acoustic pressure from the piston can be derived from the Kirchhoff–Helmholtz integral theorem [8, 9]. This formula resembles the results from the Fresnel–Kirchhoff theory of diffraction by an aperture on which a wave disturbance (plane wave or diverging spherical wave) is incident. So this is the basic problem in which basic physical mechanism can be studied from the standpoints of noise source characteristics or sound propagation phenomena. The classical theory about this problem has been mostly concerned with the farfield sound radiation patterns that vary according to the Helmholtz number of the vibrating piston. The Helmholtz number is widely used as an index that determines the characteristics of a noise source—whether it is compact or non-compact.

0022-460X/01/030423 + 21 $35.00/0

Numerical simulation of sound radiation from a vibrating circular piston without free steam was provided as one of the benchmark problems in first computational aeroacoustics workshop [10]. It is reported that short-wavelength spurious numerical waves are often generated in the regions, in which there is rapid change in the boundary condition; in other words, discontinuous boundary condition at the edge of the piston. But there is no other in-depth description in order to understand noise radiation characteristics of such discontinuous boundary condition.

In this paper, we carry out numerical simulation of sound radiation produced by an oscillating, baffled piston with three types of boundary conditions, and with various free-stream velocities by means of the DRP scheme. The objectives of this study are two-fold. The first objective is to study the effect of the piston boundary conditions, especially at the edge of the piston, on noise radiation patterns coupled with free stream. To analyze this effect, we devise three types of piston models; Gauss function, Cosine function and flat plane oscillation. The reason for selecting these oscillation types as the piston boundary conditions is that they have definite mathematical characteristics. The first is the oscillation of the piston that is continuous both in displacement and in slope at the edge of the piston. The second is the oscillation of the piston that is continuous in displacement but discontinuous in slope. The third is the vibration of the piston that is discontinuous in both. Through the comparison with numerical results of these piston models, the effects of boundary conditions at the edge of the piston on sound radiation patterns will be clearly shown. The second is to test the numerical method's ability to simulate the discontinuity effect on the sound radiation. In contrast to computational fluid dynamics (CFD), which has advanced to a fairly mature state, computational aeroacoustics (CAA) has only recently come forth as a separate area of study. Although aeroacoustics problems are governed by the same equations as those in aerodynamics, acoustic waves have their own characteristics which make computation challenging. Acoustic waves are intrinsically unsteady, and their amplitudes are several orders smaller than the mean flow and their frequencies are generally very high. Distance from the noise source to the boundary of the computation domain is also usually quite long. Thus, to ensure that computed solution is uniformly accurate over such long propagation distances, the numerical scheme must be free of numerical dispersion, dissipation and anisotropy. To satisfy these requirements, a high order numerical scheme in both space and time is generally required for CAA. High order scheme can support the spurious wave. The numerical simulation has an essentially discontinuous property. Thus, it is known, as mentioned above, that the discontinuity boundary condition in computational aeroacoustics produces spurious waves. To the author's knowledge, however, it has not been researched or discussed in depth to this day. In this paper, it is presented that the degree of discontinuity at the boundary region as well as the Helmholtz number is also an important factor in affecting the sound radiation pattern from an oscillating circular piston. Through the comparison with the analytic result obtained by integrating numerically the equation derived from Kirchhoff–Helmholtz's theorem for infinite plane surfaces [8, 9], the results of the numerical simulations for the effects of discontinuity are validated.

The linearized Euler equations in Cartesian co-ordinates are solved with the dispersion-relation-preserving (DRP) finite difference scheme over the computational domain. A number of finite difference schemes [11–14] have been proposed but the dispersion-relation-preserving (DRP) scheme of Tam and Webb [15] has proven to be quite successful in calculating linear waves for many acoustic computations [16]. The radiation and outflow boundary conditions proposed by Tam and Dong [17] are applied at the farfield boundary of the computational domain. Wall boundary conditions are applied with ghost values of pressure at the ghost points proposed by Tam and Dhong [18].

The governing equations, numerical scheme and various boundary conditions will be discussed briefly in the next two sections. The exact solution is derived for comparison with the numerical results and the classical theory is shown in section 4. The axisymmetric 2-D and 3-D numerical simulations are executed and discussion on the numerical results for the noise radiation from the oscillating piston in a free stream with three boundary types at the edge of the piston are presented in sections 5 and 6.

2. GOVERNING EQUATIONS AND NUMERICAL METHODS

The linearized Euler's equations in Cartesian co-ordinates take the following form:

$$\frac{\partial \mathbf{U}}{\partial t}+\frac{\partial \mathbf{E}}{\partial x}+\frac{\partial \mathbf{F}}{\partial y}+\frac{\partial \mathbf{G}}{\partial z}=0, \tag{1}$$

where

$$\mathbf{U}=\begin{bmatrix}\rho\\ u\\ v\\ w\\ p\end{bmatrix},\quad \mathbf{E}=\begin{bmatrix}M_x\rho+u\\ M_xu+p\\ M_xv\\ M_xw\\ M_xp+u\end{bmatrix},\quad \mathbf{F}=\begin{bmatrix}v\\ 0\\ p\\ 0\\ v\end{bmatrix},\quad \mathbf{E}=\begin{bmatrix}w\\ 0\\ 0\\ p\\ w\end{bmatrix}. \tag{2}$$

Here, M_x is the constant mean flow Mach number in the x direction. All variables are presented in non-dimensional form. The reference quantities are Δx for the length scale, c (ambient sound speed) for the velocity scale, $\Delta x/c$ for the time scale, ρ_∞ for the density scale, and $\rho_\infty c^2$ for the pressure scale.

The linearized Euler's equations in Cartesian co-ordinates are solved by the DRP finite difference scheme [15]. The DRP scheme is reviewed briefly as follows.

Let the spatial derivative be an approximation by a central difference scheme with a uniform mesh of spacing Δx as

$$\left(\frac{\partial u}{\partial x}\right)_j \approx \frac{1}{\Delta x}\sum_{l=-N}^{N} a_l u_{j+l}. \tag{3}$$

Now by applying Fourier transform to equation (3) and making use of the derivative and shifting theorems, it is found

$$\begin{aligned} \mathrm{i}k\tilde{u} &\approx \frac{1}{\Delta x}\left[\sum_{l=-N}^{N} a_l \mathrm{e}^{\mathrm{i}lk\Delta x}\right]\tilde{u} \\ &= \mathrm{i}\bar{k}\tilde{u}, \end{aligned} \tag{4}$$

where $\tilde{u}$ is the spatial Fourier transform of u and $\bar{k}$ is an effective wavenumber of the finite difference scheme:

$$\bar{k}=\frac{-\mathrm{i}}{\Delta x}\sum_{l=-N}^{N} a_l \mathrm{e}^{\mathrm{i}lk\Delta x}, \tag{5}$$

where k is the actual wavenumber, and $\mathrm{i}=\sqrt{-1}$.

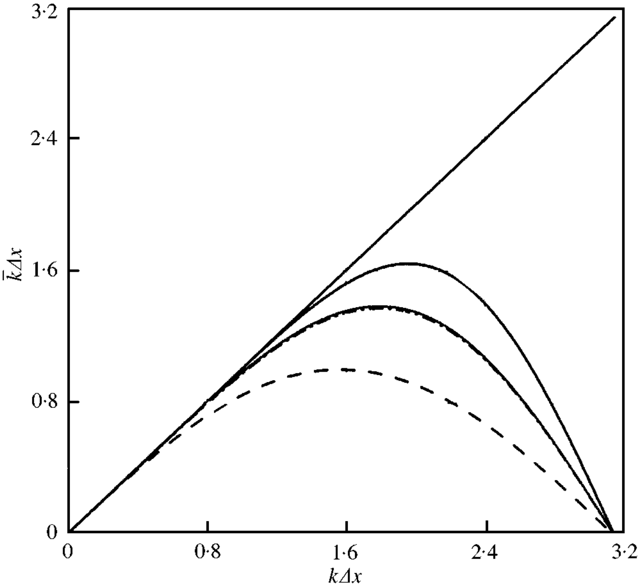

Figure 1. Numerical wave number $\bar{k}\Delta x$ versus the actual wavenumber $k\Delta x$ for several finite difference schemes: ———, 7-point fourth order DRP; ········, 5-point second order DRP; –·–·–·, 5-point fourth-order standard; — — —, 3-point second Order standard.

Thus, $\bar{k}$ of equation (5) is seen as an approximation to the actual wavenumber k. Moreover, the non-dimensionalized effective wavenumber $\bar{k}\Delta x$ as a periodic function of $k\Delta x$ with a period of 2π is a property of the finite difference scheme a_l. To assure that the Fourier transform of the finite difference scheme is a good approximation of that of the partial derivative over certain wavenumber range, it is required that a_l be chosen to minimize the integrated error, E, over certain wavenumber range, α, where

$$E = \int_0^{\alpha} |k\Delta x - \bar{k}\Delta x|^2 \, \mathrm{d}(k\Delta x). \tag{6}$$

The conditions for E to be a minimum are

$$\frac{\partial E}{\partial a_l} = 0, \quad l = 1, 2, \dots, N. \tag{7}$$

Equation (7) provides N equations for the N coefficients a_l, $l = 1, 2, \dots, N$. It is possible to combine the truncated Taylor series method and the Fourier transform optimization method. In Figure 1, $\bar{k}\Delta x$ as a function of $k\Delta x$ is plotted for several spatial discretization schemes. It is observed that $\bar{k}\Delta x$ approximates $k\Delta x$ adequately for only a limited range of the long waves. The maximum resolvable wavenumber will be denoted by critical wavenumber $\bar{k}_c$. Using the criterion $|\bar{k}\Delta x - k\Delta x| < 0{\cdot}005$, a list of $\bar{k}_c\Delta x$ values for several central difference schemes is given in Table 1. Often the resolution of spatial discretization is represented by the minimum points-per-wavelength needed to reasonably resolve the wave.

In all the following numerical simulations, we use a seven-point stencil that can be obtained by minimizing equation (6) over the integral range, $\alpha = 1{\cdot}1$ that is recommended by Tam [15]. So, the number of points-per-wavelength must be over 5·4 to acquire the reasonable accuracy of the numerical simulation.

TABLE 1

Values of critical wavenumber for several finite difference schemes of the spatial derivative

Spatial discretization	$\bar{k}_c \Delta x$	Resolution (points-per-wavelength)
7-point fourth order DRP[†]	1·163	5·40
5-point second order DRP[‡]	0·820	7·66
5-point fourth order Standard	0·682	9·21
3-point second order Standard	0·300	20·97

Note: The scheme has been optimized through minimizing the integrated error, E, over wavenumber range.
[†] $\alpha = 1{\cdot}1$.
[‡] $\alpha = 0{\cdot}9$.

Optimized four-level time discretization (Adams–Bashford method) is used as the explicit time-marching scheme [15]. To advance to the next time level, we may use the following finite difference approximation:

$$u(t + \Delta t) = u(t) + \Delta t \sum_{j=0}^{3} b_j \frac{\partial u(t - j\Delta t)}{\partial t} \tag{8}$$

By applying the Laplace transform to the above equation, we find

$$\tilde{u}\mathrm{e}^{-\mathrm{i}\omega\Delta t} = \tilde{u} + \Delta t \left(\sum_{j=0}^{3} b_j \mathrm{e}^{\mathrm{i}\omega j \Delta t} \right) \frac{\partial \tilde{u}}{\partial t}.$$

Thus,

$$-\mathrm{i}\,\frac{\mathrm{i}(\mathrm{e}^{-\mathrm{i}\omega\Delta t} - 1)}{\Delta t \sum_{j=0}^{3} b_j \mathrm{e}^{\mathrm{i}j\omega\Delta t}}\,\tilde{u} = \frac{\partial \tilde{u}}{\partial t}. \tag{9}$$

By comparing the two sides of equation (9), the quantity

$$\bar{\omega} = \frac{\mathrm{i}(\mathrm{e}^{-\mathrm{i}\omega\Delta t} - 1)}{\Delta t \sum_{j=0}^{3} b_j \mathrm{e}^{\mathrm{i}j\omega\Delta t}} \tag{10}$$

is the effective angular frequency of the time-marching scheme (8). The weighted error E_1 incurred by using $\bar{\omega}$ to approximate ω will be defined as

$$E_1 = \int_{-\zeta}^{\zeta} \{[\mathrm{Re}(\bar{\omega}\Delta t - \omega\Delta t)]^2 + (1 - \sigma)[\mathrm{Im}(\bar{\omega}\Delta t - \omega\Delta t)]^2\}\, \mathrm{d}(\omega\Delta t), \tag{11}$$

where Re( ) and Im( ) are the real and imaginary parts of ( ), σ is the weight and ς is the frequency range where we expect $\bar{\omega}$ to be a good approximation of ω. By minimizing the weighted error of equation (11), we can determine the coefficients, b_j ($j = 0, 1, 2, 3$) of equation (8). Through the stability analysis of the above time-marching scheme, it is found that Δt to be chosen such that $\bar{\omega}\Delta t < 0{\cdot}19$ guarantees numerical stability and negligible numerical damping.

With the DRP finite difference scheme, optimized 4-level time-marching scheme and the artificial damping method, the governing equations of equation (1) are discretized as

$$K^{(n)}_{l,m,k} = -\frac{1}{\Delta x}\sum_{j=-3}^{3} a_j E^{(n)}_{l+j,m,k} - \frac{1}{\Delta y}\sum_{j=-3}^{3} a_j F^{(n)}_{l,m+j,k}$$

$$-\frac{1}{\Delta z}\sum_{j=-3}^{3} a_j G^{(n)}_{l,m,k+j} \tag{12}$$

$$+\mu_a \sum_{j=-3}^{3} d_j \left(U^{(n)}_{l+j,m,k} + U^{(n)}_{l,m+j,k} + U^{(n)}_{l,m,k+j}\right),$$

$$U^{n+1}_{l,m,k} = U^{n}_{l,m,k} + \Delta t \sum_{j=0}^{3} b_j K^{(n-j)}_{l,m,k}. \tag{13}$$

The last three terms in Equation (12) are the artificial damping terms where μ_a is the artificial viscosity. All of the above coefficients can be found in reference [15].

3. BOUNDARY CONDITIONS

3.1. FARFIELD BOUNDARY CONDITION

To ensure that the computed solutions are of high-quality, farfield boundary condition must be sufficiently transparent to the outgoing disturbances so that they exit in the computation domain without much reflection. The linearized Euler equations can support three types of wave. Thus, in general, the outgoing disturbances would contain a combination of acoustic, entropy and vorticity waves each having distinct wave propagation characteristics. The acoustic wave consists of all physical variables and has its own velocity. Thus, this wave moves at the velocity equal to the vector sum of free stream and acoustic wave velocity. The entropy wave consists of density fluctuation alone. The vorticity wave consists of velocity fluctuation alone. Because both waves do not have their own velocity, they move downstream as a frozen type at the mean-flow velocity. At the outer boundary of the computational domain, radiation and outflow boundary conditions [17] are imposed. These boundary conditions are derived from the asymptotic solutions of the linearized Euler's equations. The radiation boundary condition is used at the boundary where there are only outgoing acoustic waves. On the other hand, the outflow boundary condition is used throughout the outflow region, where outgoing disturbances consisting of a combination of acoustic, entropy and vorticity waves exist. The equations are, respectively,

$$\left(\frac{1}{V(\theta)}\frac{\partial}{\partial t} + \frac{\partial}{\partial R} + \frac{1}{R}\right)\begin{bmatrix}\rho\\ u\\ v\\ w\\ p\end{bmatrix} = 0, \tag{14}$$

$$\frac{\partial \rho}{\partial t} + u_0\frac{\partial \rho}{\partial x} = \frac{1}{a_0^2}\left(\frac{\partial p}{\partial t} + u_0\frac{\partial p}{\partial x}\right),$$

$$\begin{aligned}
&\frac{\partial u}{\partial t}+u_0\frac{\partial u}{\partial x}=-\frac{1}{\rho_0}\frac{\partial p}{\partial x},\\
&\frac{\partial v}{\partial t}+u_0\frac{\partial v}{\partial x}=-\frac{1}{\rho_0}\frac{\partial p}{\partial y},\\
&\frac{\partial w}{\partial t}+u_0\frac{\partial w}{\partial x}=-\frac{1}{\rho_0}\frac{\partial p}{\partial z},\\
&\frac{1}{V(\theta)}\frac{\partial p}{\partial t}+\frac{\partial p}{\partial R}+\frac{p}{R}=0,
\end{aligned}\tag{15}$$

where $V(\theta)=c_0[M\cos\theta+(1-M^2\sin^2\theta)^{1/2}]$ and $R=\sqrt{x^2+y^2+z^2}$.

3.2. WALL BOUNDARY CONDITION

For inviscid flows the well-known boundary condition at a solid wall is that the velocity component normal to the wall is zero. This condition is sufficient for the determination of a unique solution to the Euler equations. For a high order finite difference scheme the order of the difference equations is higher than that of the Euler equations. Thus, the zero normal velocity boundary condition is insufficient for defining a unique solution. Extraneous numerical conditions must be imposed. Ghost value of pressure [18] is used as the extraneous boundary condition.

Let us consider an inviscid fluid adjacent to a solid wall at $y=0$. In this case the wall boundary condition is $v=0$ at $y=0$ where (u, v) are the velocity components in the x and y directions respectively. Since there is one boundary condition, one ghost value is needed for each boundary point at the wall. Physically, the wall exerts a pressure on the fluid with a magnitude just enough to make $v=0$ at its surface. This suggests that a ghost value in p at the ghost point immediately below the wall should be used to simulate the pressure of the wall. The ghost value of p at the ghost point $(l, -1)$ of the nth time step or $p_{l,-1}^{(n)}$ is to be chosen so that $v_{l,0}^{(n)}$ is zero for all n. This can be accomplished through the discretized form of the y-momentum equation. For more detailed descriptions see reference [18]. However, on the solid surface of a wall, the slip boundary condition $\mathbf{V}\cdot\hat{n}_{wall}=0$ is imposed and ghost values of pressure are applied as the extra boundary condition.

4. CLASSICAL THEORY AND ANALYTICAL SOLUTION

The acoustic pressure from an isolated vibrating body (or for a fixed surface enclosing a source) in an otherwise unbounded fluid can be represented by the Kirchhoff–Helmholtz integral formula [8, 9]

$$p(\mathbf{x},t)=\frac{\rho}{4\pi}\iint\frac{\dot{v}_n(\mathbf{x}_s,t-R/c)}{R}\,\mathrm{d}S+\frac{1}{4\pi c}\iint\mathbf{e}_R\cdot\mathbf{n}_s\left(\frac{\partial}{\partial t}+\frac{c}{R}\right)\frac{p(\mathbf{x}_s,t-R/c)}{R}\,\mathrm{d}S,\tag{16}$$

where $R=|\mathbf{x}-\mathbf{x}_s|$, $\mathbf{e}_R=(\mathbf{x}-\mathbf{x}_s)/R$, $\mathbf{x}_s$ is a point on the surface of the body, and $\mathbf{x}$ is a point outside the body.

A model for a source with a baffle is that a limited portion of a surface has prescribed normal velocity while the remainder of the surface being idealized as rigid. The surface is taken as $z=0$ plane and the region on the $+z$ side of the surface is idealized as unbounded.

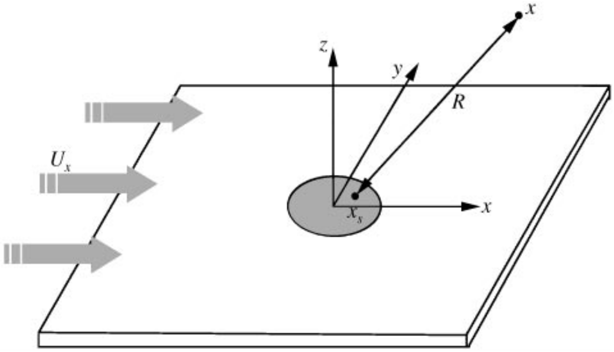

Figure 2. Nomenclature for description of radiation from a vibration circular cylinder with normal velocity $v_n(x_s, y_s, t)$.

An expression for the acoustic pressure outside the surface can be extracted from the Kirchhoff–Helmholtz integral theorem with the aid of the method of images. The boundary value problem, with non-zero $v_n(x, y, t)$ specified on some area of the $z = 0$ plane and otherwise zero, is equivalent to that of the radiation from a thin disk of time-varying thickness in an unbounded medium. The resulting z symmetry requires p, v_x, and v_y to be even with z but v_z to be odd with z. Consequently, the net contribution from surface pressure to the Kirchhoff–Helmholtz integral is zero. The integrals over the surface-normal velocity from the front and back surfaces of the disk give equal contributions, so the acoustic pressure produced by the components of the velocity normal to the $z = +0$ plane is derived from Kirchhoff–Helmholtz's theorem, as follows:

$$p(\mathbf{x}, t) = \frac{\rho}{2\pi} \iint \frac{\dot{v}_n(x_s, y_s, t - R/c)}{R} \, \mathrm{d}x_s \, \mathrm{d}y_s. \tag{17}$$

The above equation can be rewritten for convenience as follows:

$$p(\mathbf{x}, t) = \frac{\rho}{2\pi} \frac{\partial}{\partial t} \iint \left[\frac{v_n}{R} \right] \mathrm{d}x_s \, \mathrm{d}y_s, \tag{18}$$

where [ ] denotes the values at retarded time. If a piston in an infinite plane wall has a flow with a uniform velocity **U** over it and the displacement of the surface of the piston is $\xi = \xi(x_s, y_s, t)$ (Figure 2), equation (18) can be expressed as follows:

$$\begin{aligned} p(\mathbf{x}, t) &= \frac{\rho}{2\pi} \frac{\partial}{\partial t} \int_s \left[\frac{1}{R} \frac{\partial \xi}{\partial \tau} \bigg|_{\mathbf{x}_s} \right] \mathrm{d}x_s \, \mathrm{d}y_s \\ &= \frac{\rho}{2\pi} \frac{\partial}{\partial t} \int_s \frac{1}{R} \frac{\partial \xi}{\partial \tau} \bigg|_{\mathbf{x}_s} \delta(t - \tau - |\mathbf{x} - \mathbf{x}_s|/c) \, \mathrm{d}x_s \, \mathrm{d}y_s \, \mathrm{d}\tau \\ &= -\frac{\rho}{2\pi} \frac{\partial}{\partial t} \int_s \frac{\xi}{R} \frac{\partial}{\partial \tau} \delta(t - \tau - |\mathbf{x} - \mathbf{x}_s|/c) \, \mathrm{d}x_s \, \mathrm{d}y_s \, \mathrm{d}\tau \\ &= \frac{\rho}{2\pi} \frac{\partial^2}{\partial t^2} \int_s \frac{\xi}{R} \delta(t - \tau - |\mathbf{x} - \mathbf{x}_s|/c) \, \mathrm{d}x_s \, \mathrm{d}y_s \, \mathrm{d}\tau. \end{aligned} \tag{19}$$

Rewriting this integral in terms of $\eta = \mathbf{y} + \mathbf{U}\tau$ gives

$$p(\mathbf{x}, t) = \frac{\rho}{2\pi} \frac{\partial^2}{\partial t^2} \int_s \frac{\xi(\eta_1, \eta_2, \tau^*)}{R|1 + M_r|} \mathrm{d}\eta_1 \, \mathrm{d}\eta_2 \tag{20}$$

where $\mathbf{R} = |\mathbf{x} - \mathbf{x}_s(\tau^*)|$ and τ^* satisfies $c(t - \tau^*) = |x - x_s(\tau^*)|$. The sound heard by the observer at $\mathbf{x}$ and time t is emitted by the source at $\mathbf{x}_s(\tau^*)$ at time τ^*. The theoretical results can be obtained by making numerical integration of equation (20).

At points where the radial distance r is much larger than piston radius, a suitable approximation for characteristic far field is realized. In this case, R is replaced by $r - \mathbf{x}_s \cdot \mathbf{e}_r$ in the term of retarded time and by r in the denominator of equation (17) for the constant frequency case. In such a limit of large r, equation (17) is reduced to the form of an outgoing spherical wave with non-uniform directivity, as follows:

$$\hat{p} \approx f(\theta, \phi) r^{-1} \mathrm{e}^{\mathrm{i}kr}, \tag{21}$$

where we abbreviate

$$\begin{aligned} f(\theta, \phi) &= \frac{-\mathrm{i}\omega\rho}{2\pi} \iint \hat{v}_n(x_s, y_s) \mathrm{e}^{-kx_s \cdot e_r} \, \mathrm{d}x_s \, \mathrm{d}y_s \\ &= \frac{-\mathrm{i}\omega\rho}{2\pi} g(k \sin\theta \cos\phi, k \sin\theta \cos\phi). \end{aligned} \tag{22}$$

For a circular piston, where $\hat{v}_n$ is constant up to radius a and therefore zero, $f(\theta, \phi)$ reduces to

$$f(\theta) = \frac{-\mathrm{i}\omega\rho\hat{v}_n}{k^2 \sin^2\theta} \int_0^{\mathrm{ka}\sin\theta} J_0(\eta)\eta \, \mathrm{d}\eta = -\mathrm{i} \frac{\rho c \hat{v}_n \mathrm{ka}^2}{2} \frac{2J_1(\mathrm{ka}\sin\theta)}{\mathrm{ka}\sin\theta}. \tag{23}$$

The factor $2J_1(\mathrm{ka}\sin\theta)/(\mathrm{ka}\sin\theta)$, considered as a function of θ, is 1 at $\theta = 0$ and has one zero between 1 and $\pi/2$ if $3{\cdot}832 < \mathrm{ka} < 7{\cdot}016$, two zeros if $7{\cdot}016 < \mathrm{ka} < 10{\cdot}173$, three zeros if $10{\cdot}173 < \mathrm{ka} < 13{\cdot}32$, etc. The farfield intensity corresponding to equations (21) and (22) is

$$I_{r,av} = \frac{|f(\theta)|^2}{2\rho c r^2} = (I_{r,av})_{\theta=0} \left[\frac{2J_1(\mathrm{ka}\sin\theta)}{\mathrm{ka}\sin\theta}\right]^2. \tag{24}$$

So the radiation patterns are given in Figure 3. A central lobe is centered at $\theta = 0$ (θ is the angle from the axis of piston). As the Helmholtz number (ka) increases, the number of lobe is also increased. These lobes are bounded at $\theta = \pm \sin^{-1}(3{\cdot}83/\mathrm{ka})$, plus one or more side lobes. Through the above classical theory, we find that the Helmholtz number is the only factor that determines the farfield radiation patterns and characterize the noise source: There is no consideration for the effects of boundary types on the sound radiation patterns.

5. 2-D AXISYMMETRIC SIMULATIONS

First, a test simulation was performed to assess the accuracy of the schemes and boundary conditions for sound radiation from the piston of which the oscillation shape is a flat plate. If there is no free stream, the problem is axisymmetric. The governing equations for the r–x-plane where (r, x, θ) are the cylindrical co-ordinate with the origin at the center

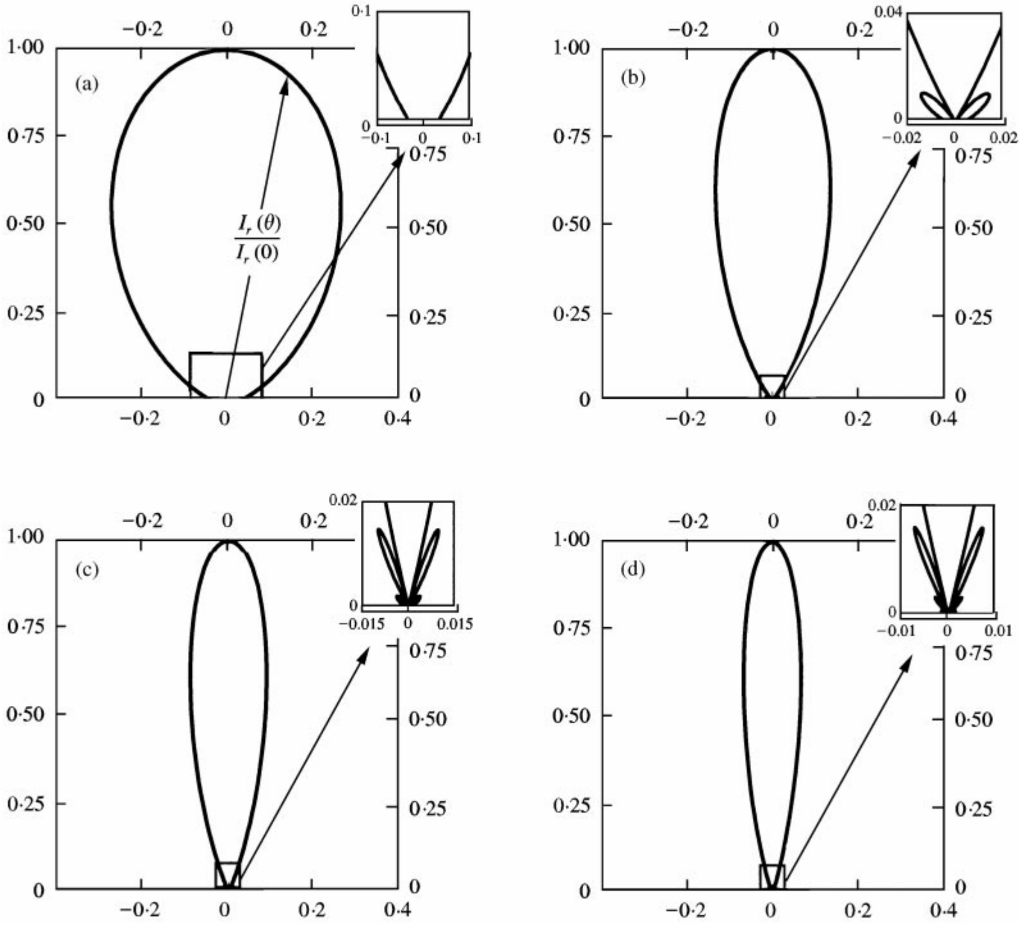

Figure 3. Farfield radiation patterns of a vibrating flat piston with various Helmholtz numbers: (a) ka $= \pi$, (b) ka $= 2\pi$, (c) ka $= 3\pi$, (d) ka $= 4\pi$.

of the piston are

$$\begin{aligned} &\frac{\partial u}{\partial t} + \frac{\partial p}{\partial x} = 0, \\ &\frac{\partial v}{\partial t} + \frac{\partial p}{\partial r} = 0, \\ &\frac{\partial p}{\partial t} + \frac{\partial v}{\partial r} + \frac{v}{r} + \frac{\partial u}{\partial x} = 0. \end{aligned} \tag{25}$$

Figure 4 shows the computation domain and boundary conditions. The normal velocity on the piston surface is set to be $u = \varepsilon_0 \sin \omega t$. The amplitude and angular frequency are set to be 10^{-4} and $0{\cdot}2\pi$ respectively. In numerical simulation, the mesh sizes are chosen to be $\Delta r = \Delta x = 1$ and the time step is $\Delta t = 0{\cdot}01$. At the axis of symmetry, $r = 0$ and equation (25) is singular. Two methods for the treatment of this singularity are used on the mesh points

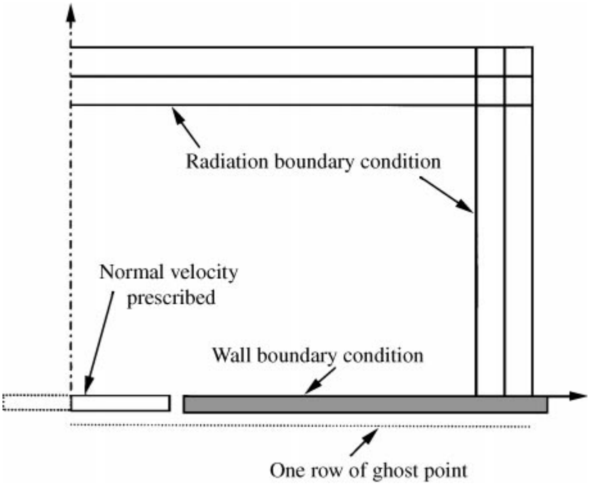

Figure 4. The computation domain and boundary conditions for 2-D-simulation.

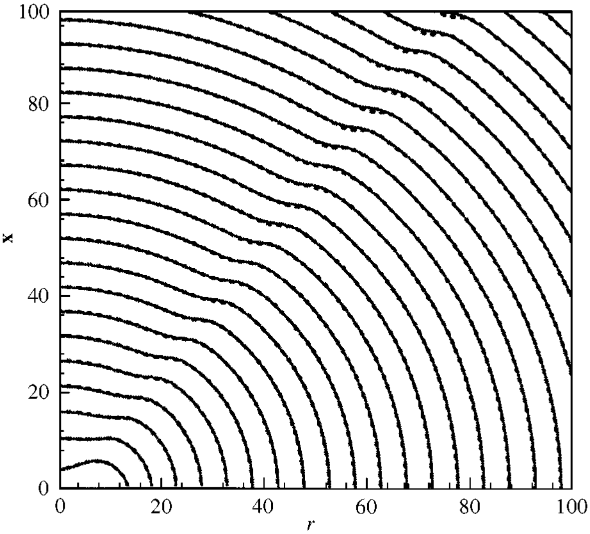

Figure 5. Zero-pressure contours ($p = 0$) at the beginning of a cycle: ———, numerical solution; · · · · · ·, exact solution.

lying on the axis of symmetry. The first is just to set the velocity v on those mesh points to be zero. The other is to substitute $\partial v/\partial r$ for v/r in equation (25). Figures 5 and 6 each show the computed zero-pressure contours ($p = 0$) at the beginning of a cycle and the computed pressure waveform along the axis of the piston at each quarter cycle respectively. It is found that they agree well with the exact solutions. This problem was provided as the first CAA benchmarking problem. In this problem, however, there is an abrupt change in the governing finite difference equations between the first two columns of mesh points on the left side of the computation domain. In addition, there is an abrupt change, i.e., discontinuity in the boundary condition at the edge of the piston. It is widely known that

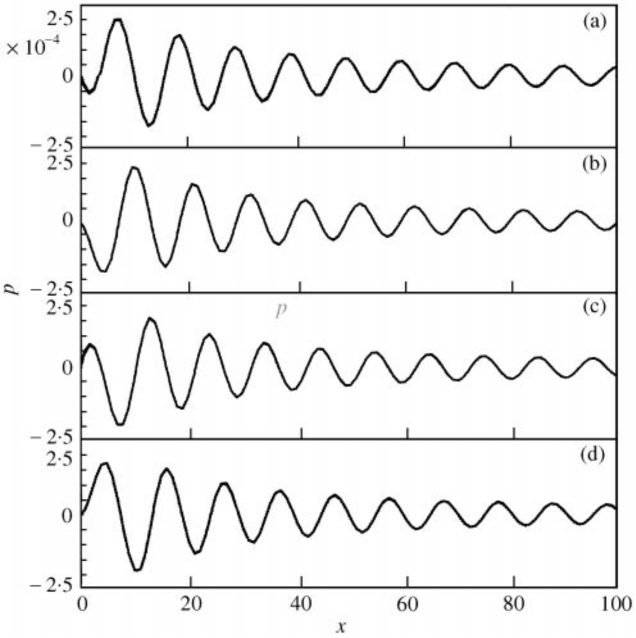

Figure 6. Pressure distribution along the axis of the piston ($r = 0$) at (a) the beginning of a cycle, (b) one-quarter of a cycle, (c) half of cycle, (d) three-quarters of a cycle: ———, numerical solution; · · · · · ·, exact solution.

short-wavelength spurious numerical waves are generated in such discontinuous regions of the computation domain. Thus, artificial viscosity term is used in the numerical computation. The numerical results in Figures 5 and 6 are calculated with optimum value of artificial viscosity. The directivity envelopes of the analytic solution and numerical solutions, which are calculated with various values of artificial viscosity, are presented in Figure 7. As the value of artificial viscosity decreases, the directivity envelope of the numerical solution approaches that of the analytic solutions. But under certain value ($\mu_a = 0{\cdot}15$) of artificial viscosity, the oscillation in the directivity envelope appears and propagates from the symmetry axis to the side directions. This oscillation is produced by spurious waves. Those spurious waves are mainly due to abrupt change in the governing finite difference equations between the mesh points on the symmetric axis and the axis-right mesh points. But there is no significant difference in the side lobe and node structures that are main points of this research. Thus, in all the following numerical simulations, the value of artificial viscosity is chosen to be as minimal as possible only if it can suppress that oscillation in the directivity envelope.

We devise three types of piston model to investigate the effects of discontinuous boundary conditions at the directivity of sound from the pistons. The schematics of these three different piston models are given in Figure 8. The boundary types of the piston include Gaussian function, cosine function and flat plate oscillation. There are all distinct mathematical characteristics of each boundary condition. For the Gaussian function oscillation, there is a continuous change in displacement and slope at the edge of the piston. For the cosine oscillation, the displacement is continuous but the slope is discontinuous at the edge of the piston. For the oscillation of the solid flat plate, both the displacement and slope are discontinuous. For convenience, the pistons with such boundary conditions are referred to as Models I, II and III respectively.

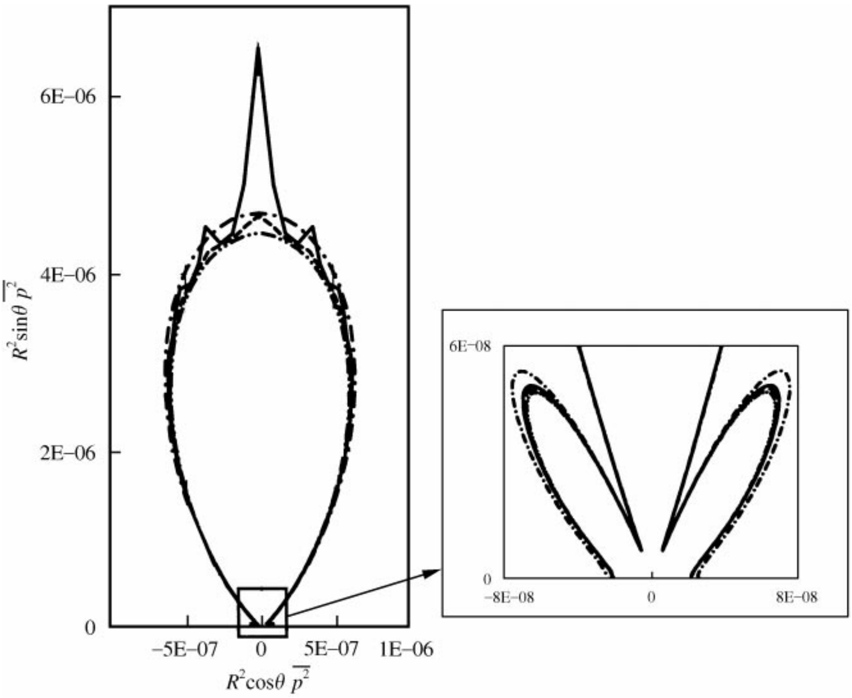

Figure 7. The directivity envelopes of the analytic and numerical results at various artificial viscosity: – · – · – · –, analytic result; ———, numeric, $\mu_a = 0{\cdot}10$; – – – – – –, numeric, $\mu_a = 0{\cdot}15$; – · · – · · numeric, $\mu_a = 0{\cdot}20$.

We carry out the numerical simulations for three piston models at several Helmholtz numbers to assess the effects of discontinuous boundary on the sound radiation. The results of the numerical simulations are shown in Figure 9. Figure 9(a) shows the directivity patterns of Model I. As the Helmholtz number of Model I increases, the magnitude of the directivity envelope also increases but the number of lobe does not change; the only one main lobe exists up to the Helmholtz number, ka $= 3\pi$. Figure 9(b) shows the directivity envelopes of Model II. The relationship between the Helmholtz number and the magnitude of the directivity envelope is the same with Model I. But the same thing cannot be said about the lobe structure. In the case of Model II, the small side lobes exist and change their direction and number as the Helmholtz number increases; two side lobes at ka $= 2\pi$ and four side lobes at ka $= 3\pi$. Model III tracks similar trends of Model II at each Helmholtz number although there are discrepancies in the direction of the side lobes. Through the comparison of numerical results of each model, we find that the discontinuity at the edge of piston as well as the Helmholtz number is an important factor in determining the sound radiation patterns.

6. 3-D SIMULATION AND DISCUSSION

If free stream is present, the problem of noise radiation from an oscillating, circular piston cannot be axisymmetric. Thus, a full 3-D numerical simulation is needed. In this section, we carry out a 3-D numerical simulation for the acoustic wave radiation from three types of pistons with several free-stream velocities. If there is no other notice, all the calculations are

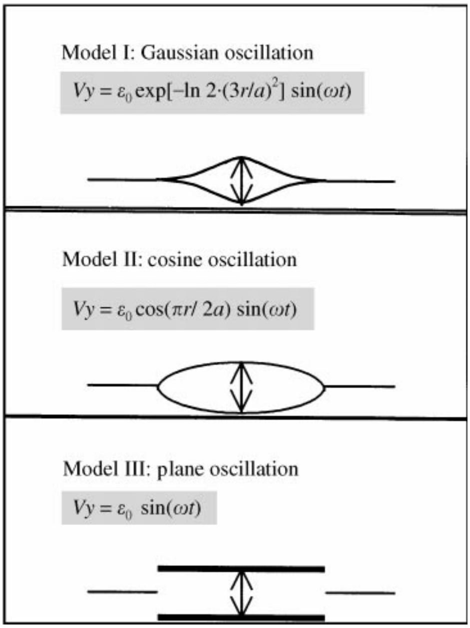

Figure 8. Three types of oscillation.

executed with the following conditions; $\Delta x = \Delta y = \Delta z = 1{\cdot}0$, $\Delta t = 0{\cdot}01$, $\omega = 0{\cdot}2\pi$, $\varepsilon_0 = 10^{-4}$, and $101 \times 101 \times 51$ grids are used.

The computational domain and various boundary conditions are given in Figure 10. Since numerical simulation is carried out with Cartesian grids, there are discrepancies between the grid lines and the boundary lines of the piston. So, artificial viscosity must be imposed primarily around the edge of the piston. The artificial viscosity is taken to be of maximum value for all mesh points lying in the semi-hemisphere region within three mesh points from the edge line of the piston. Far away from the circular line of the piston, a mesh Reynolds number is set to be of minimum value. A Gaussian distribution with a halfwidth of three mesh points is used for the maximum value of the mesh Reynolds number to the minimum. We obtain the maximum and minimum values of the artificial viscosity for each model through numerical trial and error.

We carry out all the 3-D numerical simulations with a rectangular grid to solve problems with a circular hole. This means that the boundary of the hole is not necessarily well resolved. We assume that poor grid resolution around the circular piston boundary can make numerical errors. This guess is affirmed by the grid refinement study. Figure 11 shows the pressure contours ($p = 0$) and the directivity patterns of Model I at the wall plane ($z = 0$). Figure 11(a), 11(b), and 11(c) show the pressure contours at different grid lengths; respectively, at $\Delta x = \Delta y = \Delta z = 1{\cdot}25$, $1{\cdot}0$, and $0{\cdot}625$. As the grid length becomes more refined, the numerical results show better agreement with the analytic one. Figure 11(d) shows the directivity patterns at the different grid length. The directivity envelopes in the case of $\Delta x = \Delta y = \Delta z = 1{\cdot}25$ show apparently grid-originated numerical error due to poor grid resolution around the circular piston boundary. At the grid lengths of 1·0 and 0·625, numerical results show good agreement with the analytic one. Because the boundary discontinuity of Models II and III is steeper than that of Model I, this grid-originated numerical error becomes more significant for Models II and III. Thus, the artificial viscosity

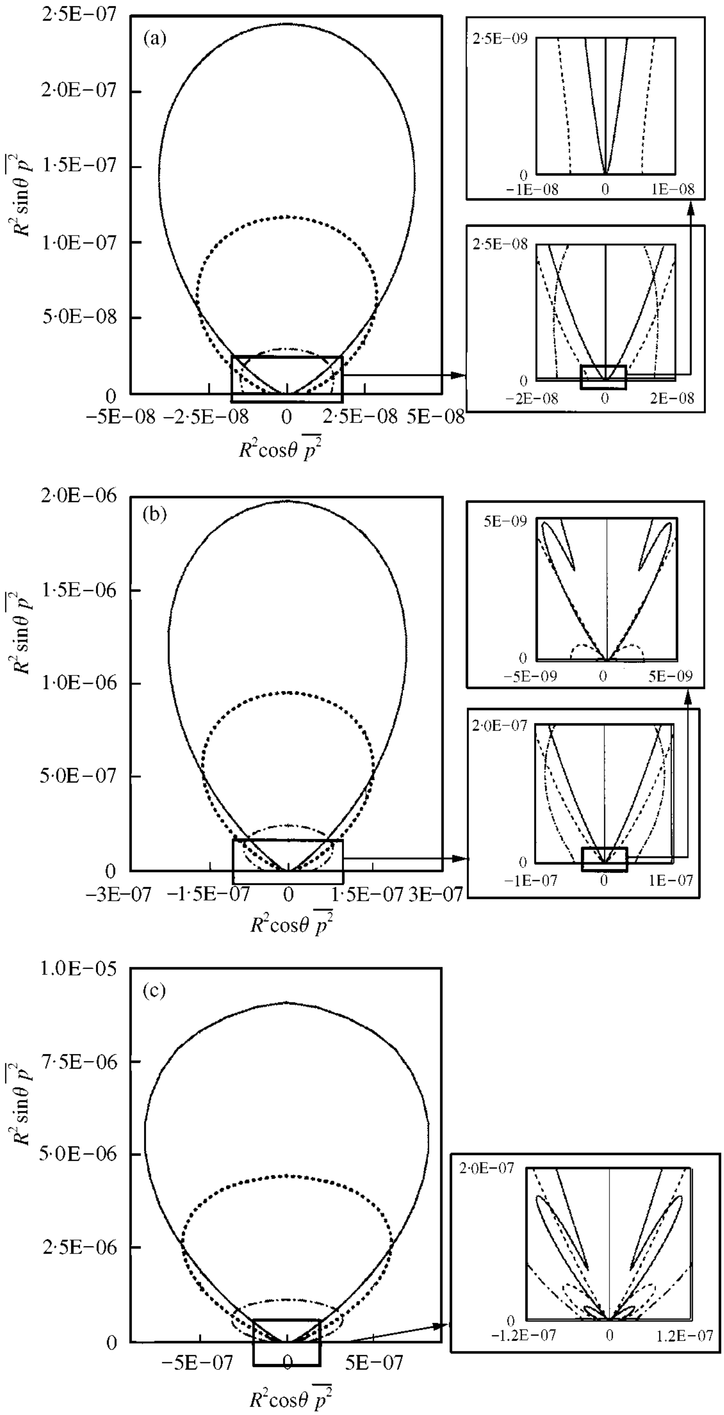

Figure 9. Directivity patterns of three piston models at several Helmholtz number: (a) Model I, (b) Model II, (c) Model III. – · – · – · –, ka = π; · · · · · ·, ka = 2π; ———, ka = 3π.

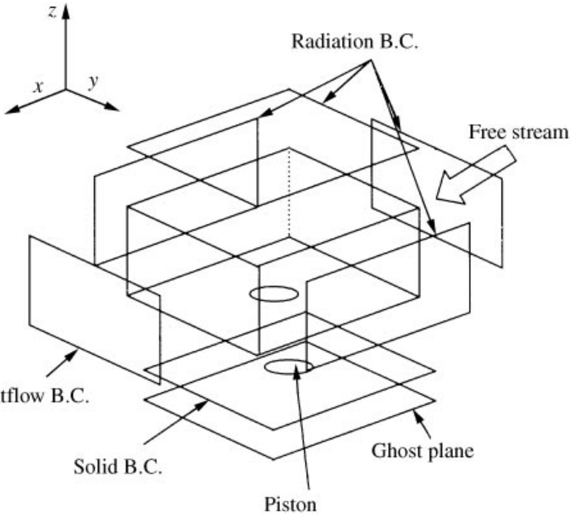

Figure 10. The computation domain and boundary conditions, Cartesian grid number (101 × 101 × 51).

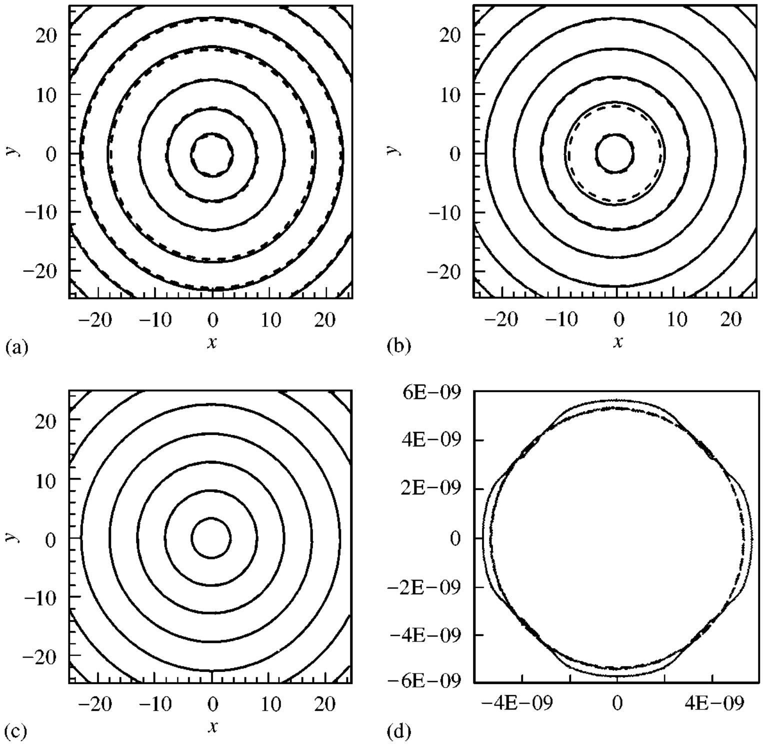

Figure 11. Pressure contours ($p = 0$) and directivity patterns at the plane of $z = 0$ from the Model I. (a) Pressure contour ($p = 0$) with $\Delta x = 1{\cdot}25$: ———, numeric; · · · · · ·, analytic. (b) Pressure contour ($p = 0$) with $\Delta x = 1{\cdot}0$: ——, numeric; · · · · · ·, analytic. (c) Pressure contour ($p = 0$) with $\Delta x = 0{\cdot}625$: ——, numeric; · · · · · ·, analytic. (d) The comparison of directivity patterns: ———, $\Delta x = 1{\cdot}25$; – · – · –, $\Delta x = 1{\cdot}0$; – – – – – – – –, $\Delta x = 0{\cdot}625$; · · · · · ·, analytic.

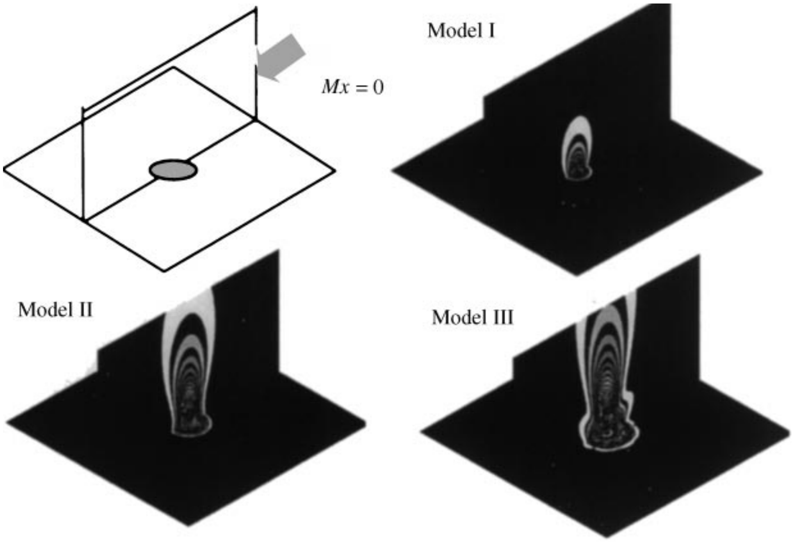

Figure 12. Mean-square pressure of each oscillation type in the plane, $y = 0$ and $z = 0$, $Mx = 0$. Model I: Gaussian, Model II: cosine, Model III: flat plane.

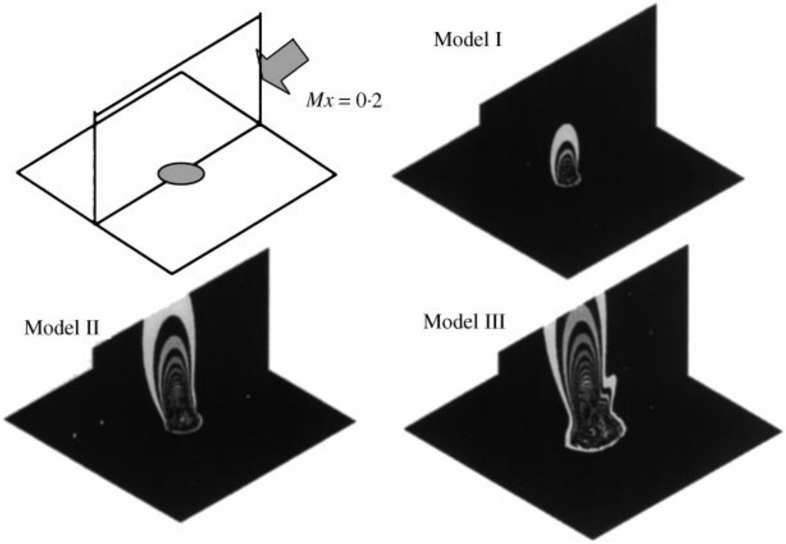

Figure 13. Mean-square pressure of each oscillation type in the plane, $y = 0$ and $z = 0$, $Mx = 0{\cdot}2$. Model I: Gaussian, Model II: cosine, Model III: flat plane.

in the simulations for these two models needs to be bigger than that of Model I. As the velocity of free stream becomes faster, this grid-originated error play a more important role in the accuracy of numerical simulation. Although we can improve the accuracy of the numerical simulation by resolving the physical domain with more grids, the computational cost would prohibitively increase in a manner similar to the cubic relation. Furthermore,

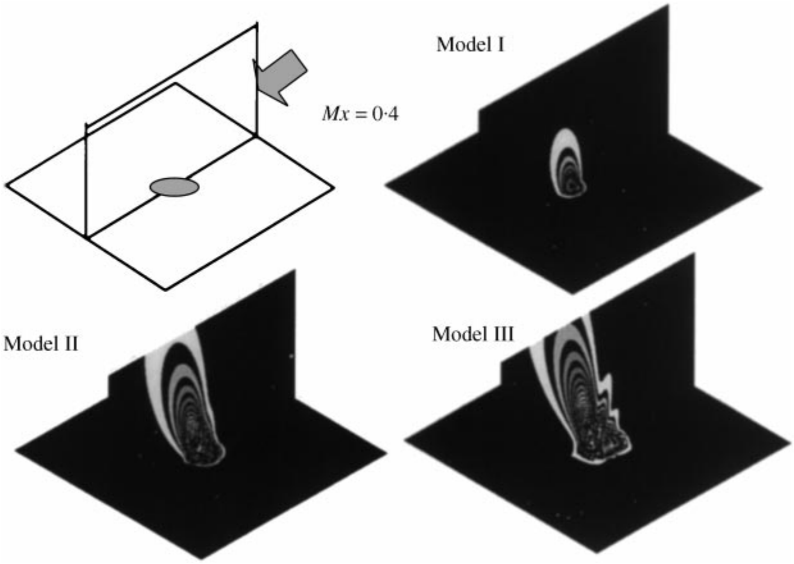

Figure 14. Mean-square pressure of each oscillation type in the plane, $y = 0$ and $z = 0$, $Mx = 0{\cdot}4$. Model I: Gaussian, Model II: cosine, Model III: flat plane.

through the comparison between the numerical and analytical results, we find that the numerical simulation with the grids of $\Delta x = \Delta y = \Delta z = 1{\cdot}0$ shows satisfactory results, similar enough to the analytic results to show the effects of discontinuous boundary conditions on the sound radiation patterns. Thus, we carry out all the following calculations with the grid resolution of $\Delta x = \Delta y = \Delta z = 1{\cdot}0$.

Figures 12–14 show the $\overline{p^2}$ contours of each piston model at the plane of $y = 0$ and $z = 0$ according to three free-stream velocities. In Figure 12, $Mx = 0$, the acoustic wave from Model I propagates mainly in the upper direction, but in Models II and III, sound propagates not only in the upper direction but also in the sideward direction despite the differences in both magnitude and direction. Such tendency of the propagation pattern of each model is maintained as free-stream velocity increases. However, it is noticed in Figures 13 and 14 that in Models II and III, not only dose the direction of sound propagation change accordingly as the free-stream velocity increases but also the number of the lobes.

To clearly show the effects of the boundary conditions on the sound radiation patterns, Figures 15–17 show the directivity pattern of each oscillation type in the $y = 0$ plane which is parallel to the free stream and perpendicular to the wall. For Model I in Figure 15, there is only one lobe in the $+z$-axis direction without node. As the free-stream velocity increases, the main lobe is inclined toward the down stream, but in Model II, it is observed that there are two extra side lobes that do not exist in Model I, although very weak, in addition to the main lobe (Figure 16). Furthermore, as the velocity of the free stream increases, the sound directivity pattern changes not only in the direction of the lobes but also in the number of lobes. The downstream lobe disappears at $Mx = 0{\cdot}2$ and the upstream lobe disappears at $Mx = 0{\cdot}3$. Sound radiation patterns of Model III are shown in Figure 17. The sound radiation patterns show a trend similar to that of Model II but side lobes exist in the upper side direction than that of Model II. Like in Model II, as the velocity of the free stream increases, both the direction of the lobes and the number of lobes change. Production of the side lobes seems to be mainly due to the difference in the boundary condition at the edge of the piston.

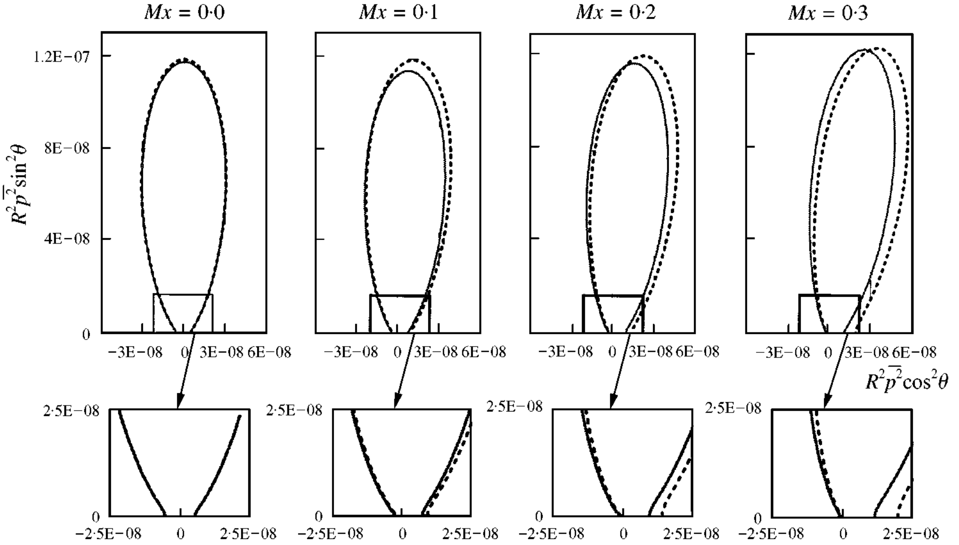

Figure 15. Directivity patterns of the Model I at several free streams: ———, numerical; · · · · · ·, analytic.

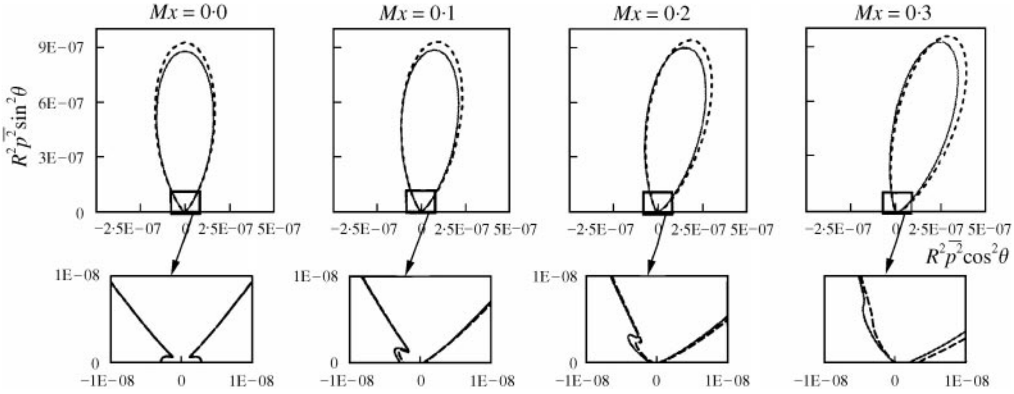

Figure 16. Directivity patterns of the Model II at several free streams: ———, numerical; · · · · · ·, analytic.

It is well known from the classical theory that as the frequency of the oscillation of the flat plate piston increases, the radiation pattern obtains many side lobes and the angular width of the major lobe becomes smaller. This study, however, shows that the velocity of the free stream coupled with the frequency and boundary condition of the piston also affect the radiation patterns of sound. There are three lobes in both Models II and III at $Mx = 0$ but the direction of the side lobes are different. As the velocity of the free stream increases, there are changes not only in the direction of the noise but also in the number of lobes. The boundary conditions of the piston at the edge of the piston coupled with free-stream velocity also change the sound radiation patterns in terms of both the direction and the number of the lobes. Via the comparison with each case, the discontinuity of the slope at the boundary between the piston and the solid wall produce side lobes and the discontinuity of the displacement causes the side lobes to go higher than the discontinuity of the slope.

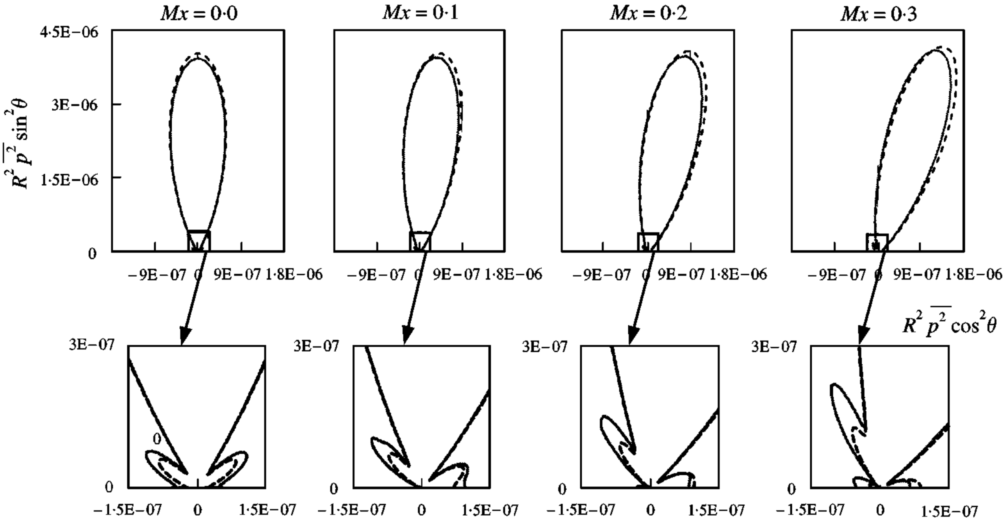

Figure 17. Directivity patterns of the Model III at several free streams: ———, numerical; · · · · ·, analytic.

7. CONCLUSION

All the numerical simulations have the essential quality of discontinuity whether physical phenomena in the real world are continuous or not. In CAA, this quality of numerical simulation is important because it may be a potential source of sound. This point is focused on through the numerical simulation.

The sound propagation from an oscillating, baffled piston in a free stream with the three types of boundary conditions at the edge of the piston was simulated numerically by using the DRP finite difference scheme.

It is not only the oscillation frequency of the piston but also the discontinuity of the boundary condition at the edge of the piston, coupled with the velocity of the free stream that affects the directivity of the sound in terms of both the direction and the number of lobes.

Through the comparison of three types of boundary conditions at the edge of the piston, it is shown that discontinuity of the slope at the edge of the piston produces side lobes. To apply this result for a more general case, a creation of the nodes in sound propagation patterns from a noise source can be partially attributed to a certain discontinuity of the sound source.

REFERENCE

1. H. LEVIN and J. SCHWINGER 1948 *Physics Review* **73**, 383–406. On the radiation of sound from an unflanged circular pipe.
2. D. L. LANSING, J. A. DRISCHLER and C. G. PUSEY 1970 *79th Spring Meeting, Acoustical Society of America, Atlantic City, NJ*, April 21–24, *Paper* 24, 9. Radiation of sound from an unflanged circular duct with flow.
3. S. D. SAVKAR 1975 *Journal of Sound and Vibration* **42**, 363–386. Radiation of cylindrical duct acoustics modes with flow mismatch.
4. R. MANI 1973 *Quarterly of Applied Mathematics* **30**, 501–519. Refraction of acoustic duct waveguide modes by exhaust Jets.

5. W. EVERSMAN 1991 *NASA Reference Publication* 1258, Vol. 2, 101. Theoretical models for duct acoustic propagation and radiation.
6. T. Z. DONG, S. H. SHIH, R. R. MANKBADI and L. A. POVINELLI 1997 3rd *AIAA/CEAS A. C.*, *AIAA*-97-1604, 12–14 May. A numerical study of duct geometry effect on radiation of engine internal noise.
7. C. K. W. TAM, *AIAA*-98-2255. Influence of nozzle geometry on the noise of high-speed Jets.
8. A. P. DOWLING and J. E. FFOWCS WILLIAMS 1983 *Sound and Sources of Sound*, 174–178. Chichester, UK: Ellis Horwood.
9. A. D. PIERCE *ACOUSTICS*, *An Introduction to its Physical Principles and Applications*, *Acoustical Society of America*, Woodbury, NY, Chapters 4 and 5.
10. J. C. HARDIN, J. R. RISTORCELLI and C. K. W. TAM 1994 *ICASE/LaRC Workshop on Benchmark Problems in Computational Aeroacoutics* (*CAA*), 24–26 October.
11. J. D. THOMAS and P. L. ROE 1993 *AIAA Paper* 93-3382. Development of non-dissipative numerical schemes for computational aeroacoustics.
12. D. W. ZINGG, H. LOMAX and H. JURGENS 1993 *AIAA Paper* 93-0459. An optimized finite difference scheme for wave propagation problems.
13. S. K. LELE 1992 *Journal of Computational Physics* **103**, 16–42. Compact finite difference schemes with spectral-like resolution.
14. J. W. KIM and D. J. LEE 1997 *CFD Journal* **5**, 281–300. Numerical simulation of nonlinear using optimized high-order compact scheme.
15. C. K. W. TAM and J. C. WEBB 1993 *Journal of Computational Physics* **107**, 301–320. Dispersion relation preserving finite difference scheme for computational aeroacoustics.
16. C. K. W. TAM, J. C. WEBB and Z. DONG 1993 *Journal of Computational Physics* **107**, 262–281. A study of the short wave components in computational acoustics.
17. C. K. W. TAM and Z. DONG 1995. *Proceedings of the First Joint AIAA/CEAS*, Hampton, VA. 12–15. Radiation and outflow boundary conditions for direct computation of acoustic and flow disturbances in a nonuniform mean flow.
18. C. K. W. TAM and Z. DONG 1994 *Theoretical and Computational Fluid Dynamics* **6**, 303–322. Wall boundary condition for high-order finite-difference schemes in computational aeroacoustics.